Aerospace Science and Technology 162 (2025) 110199

Contents lists available at ScienceDirect

Aerospace Science and Technology

journal homepage: www.elsevier.com/locate/aescte

Dynamic load alleviation of input-redundant flexible aircraft via nonlinear control allocation over invariant manifold

Boge Dong [a], Yi Zhou [a], Molong Duan [a,b,*]

[a] Department of Mechanical and Aerospace Engineering, The Hong Kong University of Science and Technology, Hong Kong, China
[b] HKUST Shenzhen-Hong Kong Collaborative Innovation Research Institute, Futian, Shenzhen, China

ARTICLE INFO

Editor: Mrinal Kumar

Keywords:
Maneuver load alleviation
Input redundancy
Flexible aircraft
Invariant manifold
Wind tunnel tests

ABSTRACT

Flexible aircraft design in modern transport aircraft improves fuel efficiency by increasing lift, reducing drag, and minimizing weight. This design increases structural flexibility, requiring special attention to load at critical locations to prevent failure during intense maneuvers or gusts. Traditional maneuver load alleviation is typically achieved through static allocation of control surface deflections or linear aeroelastic models. It is particularly challenging to separate flexible responses from rigid-body responses due to the nonlinear aerodynamic and geometric characteristics of flexible aircraft. This paper proposes a decoupled dynamic load alleviation strategy for input-redundant flexible aircraft exploiting invariant manifold structures of nonlinear systems. The nonlinear modeling considers static and periodically excited aeroelastic responses of flexible aircraft as a linear parameter-varying system with nonlinear steady-state gain, facilitating a novel nonlinear control allocation framework. This framework manipulates a proxy signal across the invariant manifold structure considering both high-frequency and low-frequency aircraft response components to minimize impact on rigid-body responses, achieving effective decoupling. The proposed nonlinear control allocation further minimizes load violation through output-input-constraint conversion. A flexible aircraft wing prototype is developed and tested through simulations and wind tunnel experiments, demonstrating enhanced load alleviation capabilities without compromising rigid-body responses compared to existing methods.

1. Introduction

Following the aviation industry's aim to cut carbon emissions by half by 2050 [1], high-aspect-ratio wings and lightweight structures are increasingly adopted in aircraft design for their enhanced lift-to-drag ratio and reduced structural weight. This design leads to an flexible aircraft (FA) design that exhibits more prominent aeroelastic responses, such as larger deformation, lower flutter speed, more prone to vibrations, and higher risks of structural divergence and failure. These aeroelastic responses are particularly intense during aggressive maneuvers or excessive gust encounters. Therefore, load alleviation methods that effectively reduce the load at critical locations on FA are needed. For load alleviation tasks, it is also desirable to preserve rigid-body tracking performance [2] to avoid conflicts with existing aircraft stabilizing augmentation systems and to enhance passenger ride comfort.

Maneuver load alleviation (MLA) techniques are broadly categorized into hardware and software-based approaches. Hardware approaches typically introduce additional mechatronics components to alleviate loads. These mechatronics components include both passive mechanisms (variable stiffness airfoils [3], morphing wings with compliant structures [4], wingtip devices [5], etc.) and active devices (piezoelectric actuators [6], variable airfoil geometries [7], and adaptive morphing devices [8], etc.). However, hardware approaches often suffer from higher design, manufacturing, assembly, and verification costs than software-based approaches.

Early software-based MLA methods focus solely on the optimization of steady-state signals or static effectors [9–12]. To further exploit dynamic aeroelastic responses, White [13] introduced symmetric control surface deflections proportional to the aircraft's acceleration to reduce loads. Yang et al. [14] enhanced this design by using multiple independent control surfaces to increase MLA efficiency. Advancements in aeroelastic modeling enabled the integration of Model predictive control (MPC) [15–18], $\mathscr{H}^\infty$ control [19], and adaptive control [20] into MLA methods. Haghighat et al. [15] proposed an MPC framework with an additional feedback loop to improve the prediction accuracy of gust load alleviation of very flexible aircraft. Liu et al. [18] incorporated MPC

* Corresponding author at: Room 2570, Academic building, The Hong Kong University of Science and Technology, Clear Water Bay, Kowloon, Hong Kong, China.
E-mail address: duan@ust.hk (M. Duan).

https://doi.org/10.1016/j.ast.2025.110199
Received 12 August 2024; Received in revised form 12 March 2025; Accepted 4 April 2025
Available online 7 April 2025
1270-9638/

Nomenclature

n	The number of control inputs
m_r	The number of rigid outputs
m_f	The number of flexible outputs
u	Control inputs
u_l	Low-frequency control inputs
u_h	High-frequency control inputs
$u_0(t)$	Control input trajectory
$u_N(t)$	Control allocation input trajectory
u_1	Inner control surface
u_2	Outer control surface
y	Flexible aircraft outputs
y_r	Rigid outputs of the flexible aircraft
y_f	Flexible outputs of the flexible aircraft
y_l	Low-frequency flexible aircraft outputs
y_h	High-frequency flexible aircraft outputs
Y_f^-	Lower saturation bound of the flexible output
Y_f^+	Upper saturation bound of the flexible output
v	Proxy signal that manipulates the flexible responses without affecting rigid responses
v_l	Proxy signal that manipulates the low-frequency flexible responses without affecting static rigid responses
v_h	Proxy signal that manipulates the high-frequency flexible responses without affecting dynamic rigid responses
$\bar{v}$	The upper bound of the proxy signal
$\underline{v}$	The lower bound of the proxy signal
$S_{\underline{v}}^{\bar{v}}$	The constraint proxy signal
T_f	Flexible selection matrix
T_r	Rigid body selection matrix
$G_h(s,\rho)$	Transfer function form of the linear parameter-varying model
f_l	Low-frequency nonlinear function that relates low-frequency inputs to low-frequency flexible aircraft outputs
$f(u_l)$	The nonlinear effectiveness in the linear parameter-varying model
J_l	The Jacobian of the low-frequency nonlinear function
μ_c	Low-frequency compensated signal
$\mu_{0,l}$	Time derivative of the low-frequency portion of the control input u_0
M_x	Out-of-plane bending moment
ρ	The flight conditions parameter
L_y	Lift force
x_h	The rigid and flexible states of the FA, as well as other states necessary to present high-frequency aerodynamic and aeroelastic effects
x_p	The internal state of the low-pass filter
x_N	The internal state of the high-frequency invariant manifold
A_p	State matrix of the low-pass filter
$A_h(\rho)$	State matrix of the linear parameter-varying model
$A_N(\rho)$	State matrix of the high-frequency invariant manifold
B_p	Input matrix of the low-pass filter
$B_h(\rho)$	Input matrix of the linear parameter-varying model
$B_N(\rho)$	Input matrix of the high-frequency invariant manifold
$B_\perp(u_l)$	Low-frequency invariant manifold
C_p	Output matrix of the low-pass filter
$C_h(\rho)$	Output matrix of the linear parameter-varying model
$C_N(\rho)$	Output matrix of the high-frequency invariant manifold

Acronyms

CA	Control allocation
CSCA	Compensated static control allocation
CNCA	Constraint nonlinear control allocation
DOF	Degree of freedom
DCA	Dynamic control allocation
FA	Flexible aircraft
FW	Flexible wing
IM	Invariant manifold
LPV-NG	Linear parameter-varying system with nonlinear DC gain
LPV	Linear parameter-varying
LTI	Linear time-invariant
MLA	Maneuver load alleviation
MPC	Model predictive control
MIMO	Multiple-input multiple-output
NURBS	Non-uniform rational B-spline
NCA	Nonlinear control allocation
OICC	Output-input constraint conversion
SISO	Single-input single-output
SMB	Static-model-based
VFA	Very flexible aircraft

with linear quadratic Gaussian to achieve an infinite prediction horizon and infinite control horizon to enhance the load alleviation performance as the gust encounters. MPC with Burlion et al. [19] introduced an $\mathscr{H}^\infty$ approach with an output saturation strategy to optimize flight tracking performance and wing-root bending moment reduction. Zhao et al. [20] utilized a least mean-squared algorithm in their adaptive controller to decrease the wing-root bending moment in a large transport airplane. However, due to the high computational cost of solving coupled dynamic models, these methods limit the use of reduced-order or linearized models. These reduced-order or linearized models are insufficient to capture the nonlinearity of the FA.

The software-based MLA drives the need for low computational cost aeroelastic models that capture the inherent geometric and aerodynamic nonlinearity of FA. Unlike traditional rigid aircraft with only 6 degree of freedoms (DOF), FA typically has hundreds or thousands of states [20, 21], due to local deformations. Previous literature widely applies linear elastic deformation to the modeling of FA. Schmidt and Raney [22] consider elastic deformation caused displacement change in the flexible vehicles modeling. Tuzcu [23] combines rigid-body aircraft equation of motion and elastic deformation-related terms to model flexible aircraft. Generally, the very flexible aircraft (VFA) exhibit more flexibility than FA, which is characterized by high aspect ratio wings [24], very flexible structure [25], and low natural frequency [26]. It leads to coupled nonlinearity in structure and aerodynamics. Carre et al. [27] established a nonlinear dynamic aeroelastic simulation toolbox for VFA. Shearer and Cesnik [28] integrated conventional 6-DOF equations of motion with aeroelastic equations to capture the nonlinear geometric behavior of VFAs. Duan et al. [29,30] proposed a reduced-order model combining conventional rigid-body 6-DOF equations, nonlinear structural dynamics, and data-driven low-order aerodynamics to describe VFA. However, these methods require high development costs and lack direct compatibility with the experimental data.

One unique opportunity to achieve MLA arises from the increased redundancy in modern aircraft design. This increased number of inputs enables the load alleviation to be decoupled from the rigid-body tracking control. Zink et al. [31] optimized aircraft trim solutions while reducing wing root bending moments. Frost et al. [32] developed a load alleviation framework incorporating structural load feedback. Hansen et al. [33] utilized a dynamic null space filter for a linear parameter-varying system. Zaccarian [34] proposed a static-model-based (SMB) allocator for nonlinear systems to achieve additional control objectives. However, existing approaches only address static or dynamic input-redundant systems, limiting their ability to simultaneously achieve precise control allocation for steady-state accuracy and handle high-frequency dynamics.

To overcome these limitations, a novel constraint nonlinear control allocation (CNCA) method is proposed to enhance MLA performance. Compared with existing methods, the core contributions are:

- An linear parameter-varying system with nonlinear DC gain (LPV-NG) is proposed that preserves the dynamic properties of FA through conventional linear parameter-varying (LPV) models while capturing low-frequency nonlinearity via static nonlinear functions. It is also conveniently acquired from experimental data.
- A decomposed invariant manifold (IM) structure is conveniently constructed from experimental data. IM aligns with the LPV-NG system while ensuring effective decoupling control allocation with minimal impact on the FA's rigid-body responses.
- A CNCA framework is established to enhance MLA performance by minimizing flexible load violation and enhancing resistance to high-frequency disturbances.
- The proposed method is verified in simulations and wind tunnel experiments on a flexible wing (FW) prototype.

The paper is organized as follows: Section 2 proposes the LPV-NG system, which describes the static and dynamic properties of the FA. Section 3 details the establishment of IM for a special LPV-NG system. Section 4 illustrates the FW design as a classic representation of FA, including wind tunnel tests for model construction and the load alleviation (LA) verification of proposed methods via simulation and wind tunnel tests.

2. Flexible aircraft modeling as the linear parameter-varying system with nonlinear DC gain

Increased flexibility reduces the frequency separation between rigid-body and flexible modes, intensifying interactions between flight control systems and structural dynamics. While the frequency separation assumption fails for VFA with elastic mode frequencies below 2.5 Hz [26] and requires fully coupled dynamic modeling [35], it remains valid for FA, where aeroelastic modes typically exceed 6 Hz [36]. This study focuses on FA, considering the frequency separation assumption as a reliable modeling simplification. Consider an FA is actuated by n control inputs $u \in \mathbb{R}^n$ (i.e., control surfaces and thrust forces). The output of the FA consists of m_r rigid outputs (i.e., translational and rotational velocities, lift, drag, etc.), written as y_r, as well as additional m_f flexible outputs describing the overall aeroelastic behavior defined as y_f, i.e.,

$$y = \left\{ y_f \quad y_r \right\}^\top. \tag{1}$$

General flexible outputs y_f are typically of high order to describe the overall flexible response. However, in practical settings, the reduced-order load at critical locations, such as the wing root, plays an important role in evaluating the aircraft load. This work considers this reduced-order flexible responses description, i.e., the y_f, as the standard to set up safety margins for the dynamic model.

The dynamic modeling of FA is challenging due to its nonlinearity, which is dependent on flight conditions. Moreover, it is challenging to find a unified dynamic model that combines static and dynamic data acquired from static and periodically excited wind tunnel experiments. Accurately modeling the unified behavior of flexible aircraft, encompassing both static and dynamic responses, presents significant challenges for physics-based theoretical modeling, such as Newtonian-Lagrangian modeling [37], strain-based beam finite element modeling [35], and reduced-order modeling [38]. To address these issues, the work proposes an LPV-NG dynamic model that describes both the static and dynamic aircraft responses. The key in the LPV-NG dynamic model is the decomposition of high-frequency and low-frequency parts of input and outputs, i.e.,

$$\begin{aligned} u &= u_l + u_h, \\ y &= y_l + y_h. \end{aligned} \tag{2}$$

The low-frequency input-to-output relationship is assumed to follow a nonlinear function $f_l(\cdot)$, which is defined as

$$y_l = f_l(u_l). \tag{3}$$

The high-frequency dynamic relationship is described as a strictly proper LPV system. It can be derived from physics-based modeling or identified directly through integration with conventional aeroelastic tests, facilitating its efficient extraction from experimental data. The LPV model is expressed in state space form, i.e.,

$$\dot{x}_h = A_h(\rho)x_h + B_h(\rho)u_h, y_h = C_h(\rho)x_h. \tag{4}$$

Define the equivalent transfer function of the LPV model as $G_h(s,\rho)$. To ensure the compatibility of the static model and this LPV system, the DC gain of the LPV system should equal the gradients of the static nonlinear function, i.e.,

$$G_h(0,\rho) = J_l(u_l) = \frac{\partial f_l(u_l)}{\partial u_l}. \tag{5}$$

Assume the low-frequency part of the input signal is acquired via a low-pass filter. It's defined in state space form as

$$\dot{x}_p = A_p x_p + B_p u, u_l = C_p x_p. \tag{6}$$

The overall decomposition defines a practical LPV-NG system in the following form

$$\begin{aligned} &\begin{Bmatrix} \dot{x}_h \\ \dot{x}_p \end{Bmatrix} = \begin{bmatrix} A_h & -B_h C_p \\ 0 & A_p \end{bmatrix} \begin{Bmatrix} x_h \\ x_p \end{Bmatrix} + \begin{bmatrix} B_h \\ B_p \end{bmatrix} u, \\ &y = \begin{bmatrix} C_h & 0 \end{bmatrix} \begin{Bmatrix} x_h \\ x_p \end{Bmatrix} + f_l(C_p x_p). \end{aligned} \tag{7}$$

The parameter ρ is omitted in the Eq. (7) for conciseness. The LPV-NG system's benefit is capturing the aircraft's static nonlinearity using nonlinear functions while preserving dynamic response with the LPV model. It also allows convenient acquisition of the static relationship and LPV matrices through static wind tunnel tests and local linear system identification.

3. Dynamic load alleviation of flexible aircraft exploiting invariant manifold

3.1. Input redundancy in the flexible aircraft

Modern transport aircraft are typically designed with input redundancy for enhanced flight safety under actuator faults. Input redundancy typically means that the aircraft has more control inputs than its rigid-body outputs [2]. This definition is also preserved in the modeling of FA, i.e.,

$$n > m_r. \tag{8}$$

Input redundancy is usually exploited in the flight control system, where the force and moment are first generated, and then redistributed through control effectors, such as control surfaces. Mathematically, input redundancy is classified as strong and weak input redundancy [39]. Strong input redundancy requires the control input to counteract each other such that the system's internal states are not affected and is typically embraced in rigid aircraft control systems. However, the strong input redundancy normally fails in handling the FA since the redistributed force and moments at different control effectors will inevitably introduce flexible responses and aircraft deformations [33]. To address these issues, weak input redundancy is more appropriate as it allows the system's internal states to be affected in the control allocation process while keeping rigid output unchanged. In this work, the input redundancy specified in Eq. (8) is a standard weak input redundancy definition. This framework enables the additional control objectives apart from the rigid-body control [40]: the structural loads at critical locations of FA are chosen to be alleviated.

3.2. Invariant manifold structure parameterized with proxy signal

The flight control system of an FA is expected to satisfy both rigid-body trajectory tracking as well as the objective of alleviating the loads at critical locations. However, the FA rigid and flexible outputs are typically coupled, and the introduction of LA typically will also affect the rigid-body responses, not conducive to passenger ride comfort. It is desirable to decouple the LA functionalities with the rigid body tracking [33,40], but the nonlinearities in the FA models pose challenges. In this work, this decoupling is achieved by allocating control input exploiting the IM specified by the FA's LPV-NG model. Specifically, consider the allocation of the control input trajectory following

$$u(t) = u_0(t) + u_N(t). \tag{9}$$

Consider the FA responds to both $u_0(t)$ and $u(t)$. The desirable decoupling of the rigid-body and flexible response requires

$$\begin{aligned} y_r(u_0) &= y_r(u), \\ y_f(u_0) &\neq y_f(u). \end{aligned} \tag{10}$$

This indicates an invariant manifold considering the rigid-body dynamic responses. To effectively allocate the allocated input u_N to satisfy Eq. (10) under the LPV-NG framework, the invariant manifold is established separately from the analysis of its low-frequency and high-frequency parts by indicating with subscript l and h respectively. The low-frequency signals appearing in the paper are obtained by applying a low-pass filter to the original signal.

The low-frequency portion of the allocated control $u_{N,l}$ is expected to satisfy

$$T_r f_l(u_{0,l}) = T_r\, f_l(u_{0,l} + u_{N,l}), \tag{11}$$

where the selection matrix is defined as

$$\begin{aligned} T_f &= \begin{bmatrix} I_{m_f} & 0_{m_f\times m_r} \end{bmatrix}, \\ T_r &= \begin{bmatrix} 0_{m_r\times m_f} & I_{m_r} \end{bmatrix}. \end{aligned} \tag{12}$$

To ensure that the low-frequency rigid outputs are invariant, $u_{N,l}$ is constructed with

$$\dot{u}_{N,l} = B_\perp(u_l)v_l + \mu_c, B_\perp(u_l) = \mathrm{Ker}\left(T_r\frac{\partial f_l(u_l)}{\partial u_l}\right), \tag{13}$$

where $\mathrm{Ker}(\cdot)$ marks the null space of a fat matrix. It is guaranteed by the weak input redundancy condition as $n > m_r$. The proxy signal $v_l(t)$ is typically selected to be a low-frequency signal to satisfy the decomposition of the LPV-NG framework defined in Eq. (7). Moreover, the μ_c will be zero when the control input trajectory u_0 is the steady value. The compensation term $\mu_c(t)$ is obtained from the time derivative of Eq. (11) that

$$\begin{aligned} \mu_c(t) = {} & J_l(u_{0,l} + u_{N,l})^{-1} T_r^{\dagger} T_r J_l(u_{0,l})\mu_{0,l} \\ & - J_l(u_{0,l} + u_{N,l})^{-1} T_r^{\dagger} T_r J_l(u_{0,l} + u_{N,l})\mu_{0,l}, \end{aligned} \tag{14}$$

where $(\cdot)^{\dagger}$ denotes the right pseudoinverse of a matrix.

The high-frequency portion of the allocated signal $u_{N,h}$ is expected to satisfy

$$T_r G_h(s,\rho) u_{N,h} = 0. \tag{15}$$

Note that $T_r G_h(s,\rho)$ represents the high frequency of the rigid output, and is a fat transfer function matrix as the redundancy condition in Eq. (8) specifies. Accordingly, it can be decomposed via matrix fraction description, i.e.,

$$T_r G_h(s,\rho) = D_h^{-1}(s,\rho) N_h(s,\rho). \tag{16}$$

Note that the numerator matrix $N_h(s,\rho)$ is also a fat matrix; therefore, its right null space is conveniently constructed as

$$N_N(s,\rho) = \mathrm{Ker}(N_h(s,\rho)), \tag{17}$$

satisfying

$$N_h(s,\rho) N_N(s,\rho) = 0. \tag{18}$$

The direct matrix fraction description in Eq. (16) may not guarantee that $D_h(s,\rho)$ yields stable poles. Thus, in practical setups, a different stable denominator matrix $D_N(s,\rho)$ can be adopted. With this formulation, it verifies that an LPV system given by

$$G_N(s,\rho) = N_N(s,\rho) D_N(s,\rho)^{-1}, \tag{19}$$

yields zero responses to the system because of the relationship

$$\begin{aligned} & T_r G_h(s,\rho) u_{N,h} = \\ & D_h^{-1}(s,\rho) \underbrace{N_h(s,\rho) N_N(s,\rho)}_{=0} D_N(s,\rho)^{-1} v_h = 0 \end{aligned} \tag{20}$$

To connect with decomposition in Eq. (2), the low-frequency and high-frequency proxy signal satisfy $v = v_l + v_h$. Define a state space realization of the high-frequency invariant manifold $G_N(s,\rho)$ as

$$\begin{aligned} \dot{x}_N &= A_N(\rho) x_N + B_N(\rho) v_h, \\ u_{N,h} &= C_N(\rho) x_N. \end{aligned} \tag{21}$$

The overall IM of FA includes the static IM $B_\perp(u_l)$, static compensator μ_c, and dynamic IM $G_N(s,\rho)$. They are combined as

$$\begin{aligned} \dot{x}_d &= \widetilde{A}_N x_d + \widetilde{B}_{N1} v + \widetilde{B}_{N2} \{ u_0 \quad \mu_0 \}^\top, \\ u_N &= \widetilde{C}_N x_d, \end{aligned} \tag{22}$$

where system state $x_d = \{ x_N \quad u_{N,l} \quad x_{u_0} \quad x_{\mu_0} \quad x_v \}^\top$, and state-space matrices are

$$\begin{aligned} \widetilde{A}_N &= \begin{bmatrix} A_N & 0 & 0 & 0 & -B_N C_p \\ 0 & 0 & 0 & \dfrac{\mu_c}{x_{\mu_0}} & B_\perp C_p \\ 0 & 0 & A_p & 0 & 0 \\ 0 & 0 & 0 & A_p & 0 \\ 0 & 0 & 0 & 0 & A_p \end{bmatrix}, \\ \widetilde{B}_{N1} &= \begin{bmatrix} B_N \\ 0 \\ 0 \\ 0 \\ B_p \end{bmatrix}, \widetilde{B}_{N2} = \begin{bmatrix} 0 & 0 \\ 0 & 0 \\ B_p & 0 \\ 0 & B_p \\ 0 & 0 \end{bmatrix}, \\ \widetilde{C}_N &= [\, C_N \quad I \quad 0 \quad 0 \quad 0 \,], \end{aligned} \tag{23}$$

where variables x_{u_0}, x_{μ_0}, and x_v are the state of the low pass filter for the u_0, μ_0, and v respectively. The parameter ρ is omitted in the Eq. (23) for conciseness. The formal expression in Eq. (22) highlights that v is the manipulated variable, and $\{u_0 \ \mu_0\}^\top$ is considered a system disturbance. It enables an IM to naturally yield allocated input u_N to guarantee the invariance of FA rigid responses as specified in Eq. (10). The proposed decoupled method improves control allocation performance by allowing to use nonlinear model to capture nonlinearity in the FA.

To address the robustness of the null space, the FA model is identified directly from static and dynamic wind tunnel experiment data, ensuring that the model accurately represents both the static magnitudes and dynamic system behavior observed in the experiments. While the identified model effectively captures the static and dynamic responses, discrepancies may still occur due to factors such as variations in experimental setup, environmental conditions, or unmodeled nonlinearities. The proposed framework addresses discrepancies by incorporating a fault detection mechanism to monitor significant deviations from expected null space behavior. When such deviations are detected, the null space is temporarily disengaged, activating an error mitigation strategy. The block diagram in Fig. 1 illustrates the proposed fault detection mechanism.

3.3. Constrained allocation exploiting the invariant manifold

Once the IM is established, the proxy signal v is manipulated to affect the flexible outputs of FA without altering the rigid response. Consider the control input u_0 is generated from the pilot or conventional aircraft controller. The LA feedback controller takes flexible output as input and is defined as

$$v = C\left(r - y_f\right), \tag{24}$$

where C is a conventional controller, whose sign depends on the effectiveness at individual channels from v to y_f. Term r is a desirable flexible response reference. The proposed nonlinear control allocation (NCA) method is established at this stage. Generally, NCA would be activated once the flexible load exceeds the desirable flexible response reference. It inevitably leads to unwanted load violations, which degrade overall FA safety. To further reduce the occurrence of the load violation, the CNCA method is proposed via Output-input constraint conversion (OICC) [41] such that the constraints on y_f is converted to the proxy signal v. The block diagram of the proposed CNCA is shown in Fig. 1.

Assume the FA's flexible output y_f satisfy the saturation bounds given by

$$Y_f^- \le y_f \le Y_f^+. \tag{25}$$

The proxy signal v is manipulated to ensure flexible output y_f remains in the constraint. Consider the unified LPV-NG system description of FA under the IM structure given by

$$\begin{aligned} \dot{x}_e &= A_w x_e + B_{w1} v + B_{w2}\{\, u_0 \quad \mu_0 \,\}^\top, \\ y_f &= C_w x_e + f_l(u_l), \end{aligned} \tag{26}$$

where $x_e = \{x_h\ x_z\ u_l\ x_{u_0}\ x_{\mu_0}\ x_v\}^\top$, and state-space matrices are

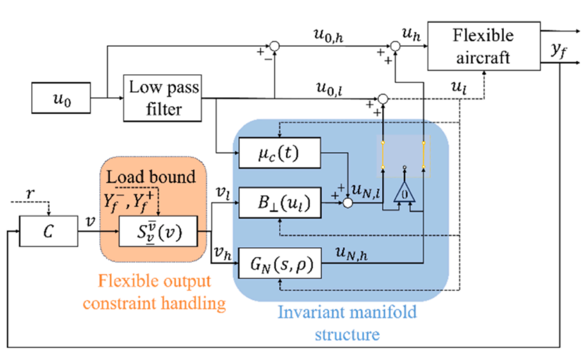

Fig. 1. Block diagram of dynamic load alleviation of flexible aircraft through proposed invariant manifold structure and flexible output constraint.

expressed as

$$\begin{aligned} A_w &= \begin{bmatrix} A & 0 & 0 & -BC_p & 0 & 0 \\ 0 & A_z & 0 & 0 & 0 & -B_z C_p \\ 0 & 0 & 0 & 0 & \widetilde{\mu}_c & B_\perp C_p \\ 0 & 0 & 0 & A_p & 0 & 0 \\ 0 & 0 & 0 & 0 & A_p & 0 \\ 0 & 0 & 0 & 0 & 0 & A_p \end{bmatrix}, \\ B_{w1} &= \begin{bmatrix} 0 \\ B_z \\ 0 \\ 0 \\ 0 \\ B_p \end{bmatrix}, B_{w2} = \begin{bmatrix} B & 0 \\ 0 & 0 \\ 0 & 0 \\ B_p & 0 \\ 0 & B_p \\ 0 & 0 \end{bmatrix}, \\ C_w &= [\, C \quad C_z \quad 0 \quad 0 \quad 0 \quad 0 \,], \end{aligned} \tag{27}$$

where A_z, B_z, and C_z are the matrices of the state space realization of $T_r G_h(s,\rho) G_N(s,\rho)$, respectively. The static compensation term is defined as $\widetilde{\mu}_c = \mu_c / x_{\mu_0} + C_l$. The system is rewritten as the general form for OICC derivation as

$$\begin{aligned} \dot{x}(x,\rho) &= f(x,\rho) + g_1(\rho) v + g_2(\rho) d, \\ y_f(x,\rho) &= c_1(x,\rho) + c_2(u_l), \end{aligned} \tag{28}$$

where d is considered as the system disturbance, and assuming the maximum disturbance magnitude is known and it is expressed as M

$$|d(t)| \le M(t). \tag{29}$$

Two nonlinear functions $\underline{v}\left(x,\rho,M,Y_f^-,Y_f^+\right)$ and $\overline{v}\left(x,\rho,M,Y_f^-,Y_f^+\right)$ need to be found that ensure v belongs to $[\underline{v},\overline{v}]$, and the flexible output y_f within the interval $\left[Y_f^-,Y_f^+\right]$. The relative degree r_1 and r_2, marked by the first nonzero Markov parameters, are each defined as the smallest integer satisfying

$$\begin{aligned} &\forall x, \forall i < r_1 - 1 \begin{cases} L_{g_1} L_f^i y_f(x,\rho) = 0, \\ L_{g_1} L_f^{r_1 - 1} y_f(x,\rho) > 0, \end{cases} \\ &\forall x, \forall i < r_2 - 1 \begin{cases} L_{g_2} L_f^i y_f(x,\rho) = 0, \\ L_{g_2} L_f^{r_2 - 1} y_f(x,\rho) > 0, \end{cases} \end{aligned} \tag{30}$$

where the symbol $L_M^j N$ is the jth Lie derivative of N along M. Define experience parameters K_{s_1}, and K_{s_2} to be positive constants. Then the time-varying positive gain K_s is given by

$$K_s(t) = \frac{K_{s_1} + 2M(t)\varepsilon(x,\rho)}{K_{s_2}\left(Y_f^+ - Y_f^-\right)}, \tag{31}$$

where $\varepsilon(x,\rho)$ is defined as

$$\varepsilon(x,\rho) = \sum_{i=1}^{r_2} L_{g_2} L_f^{i-1} y_f(x,\rho). \tag{32}$$

Term $\varepsilon(x,\rho)$ is to relate the disturbance effect on the flexible load. With relative degree and positive gain determined, constraints associated with y_f will be enforced by v for a given x, i.e.

$$\begin{cases} B^-(t,x,\rho) \le h(t,x,\rho) + h_{g_1}(t,x,\rho) v, \\ h(t,x,\rho) + h_{g_1}(t,x,\rho) v \le B^+(t,x,\rho), \end{cases} \tag{33}$$

where $B^\pm(t,x,\rho)$, $h(t,x,\rho)$, and $h_{g_1}(t,x,\rho)$are defined as

$$
\begin{aligned}
B^{\pm}(t,x,\rho) &= K_s(t)Y_f^{\pm} \mp M(t)\varepsilon(x,\rho),\\
h(t,x,\rho) &= K_s(t)\sum_{i=0}^{r_1} L_f^{r_1} y_f(x,\rho),\\
h_{g_1}(t,x,\rho) &= K_s(t)\sum_{i=0}^{r_1} L_{g_1}L_f^{r_1} y_f(x,\rho).
\end{aligned}
\tag{34}
$$

The initial condition of the nonlinear transfer function must satisfy

$$
\begin{aligned}
&Y_f^-(0) \le y_f(x_0,\rho) \le Y_f^+(0);\\
&B^-(0,x_0,\rho) \le h(0,x_0,\rho) \le B^+(0,x_0,\rho).
\end{aligned}
\tag{35}
$$

Thus, the saturation bounds on the flexible output are indirectly satisfied by imposing constraints on ν as

$$
\begin{aligned}
\overline{\nu} &= \frac{K_s(t)\left(Y_f^+ - \sum L_f^i y_f(x,\rho)\right) - \widetilde{M}}{L_{g_1}L_f^{r_1-1}y_f(x,\rho)},\\
\underline{\nu} &= \frac{K_s(t)\left(Y_f^- - \sum L_f^i y_f(x,\rho)\right) + \widetilde{M}}{L_{g_1}L_f^{r_1-1}y_f(x,\rho)}.
\end{aligned}
\tag{36}
$$

The variable is defined as $\widetilde{M} = M(t)\varepsilon(x,\rho)$. In practical applications, the saturation is specified as

$$
S_{\underline{\nu}}^{\overline{\nu}}(\nu) := \max\left(\min\left(\underline{\nu},\overline{\nu}\right),\min(\nu,\nu_m)\right),
\tag{37}
$$

where $\nu_m = \max(\underline{\nu}, \overline{\nu})$. With flexible saturation defined, the CNCA framework is established to minimize flexible output load violation while maintaining rigid output unchanged to enhance the overall flight safety of FA.

4. Flexible wing modeling and verification through simulation and wind tunnel tests

4.1. Flexible wing design and calibration

To verify the proposed control allocation method, a FW prototype was designed, fabricated, assembled, and controlled. The FW consisted of four airfoil sections, each having a 97 mm span and 100 mm chord length, connected by a central aluminum beam. Two outermost airfoil sections were equipped with additional control surfaces capable of $\pm 20^\circ$ deflection. The wind tunnel experiments were conducted at the wind tunnel of the Aerodynamic and Acoustics Facility (AAF) at The Hong Kong University of Science and Technology (HKUST). The flexible wing prototype parameters and wind tunnel installation are presented in Table 1 and Fig. 2 respectively. The FW prototype comprised two Feetech FT2304M digital servos on the outermost two airfoil sections and a Hypersen HPS-FT060E load cell at the wing root. Their specifications are summarized in Table 2 and Table 3.

The load cell measures shear force and bending moment at the wing root. The difference between lift and shear force is negligible in the low-frequency vibration and steady-flow wind tunnel experiment cases [42]. In static cases, the measured shear force equals the lift, which is the sum of aerodynamic forces perpendicular to the airfoil surface. In dynamic cases, the measurement also includes inertia forces from vibration. In this study, the vibration frequency and magnitude are small, thus, inertia forces are generally negligible compared to the lift [43]. Although using load cells to measure wing root bending moments is impractical for commercial aircraft, reconstruction is achievable with strain gauges and optical fiber strain sensors through estimation algorithms. Placement optimization techniques, such as uncertainty reduction [44], and shape-sensing improvements [45], further enhance reconstruction precision. Methods like the inverse finite element method (iFEM) [46] and KO displacement theory [47] enable structural deflection reconstruction and wing root bending moment estimation. By integrating these estimation techniques, the proposed load alleviation algorithm facilitates effective real-time load alleviation during flight operations. Thus, load cells remain a practical simplification for laboratory conditions.

Table 1
Flexible wing prototype parameters.

Parameters	Value
Semi-span	395 mm
Chord length	100 mm
Aspect ratio	7.9
Airfoil type	NACA 0021
Control surface chord length	20 mm
Central beam width	30 mm
Central beam thickness	1.5 mm
Flexibility	15% maximal deformation of semi-span

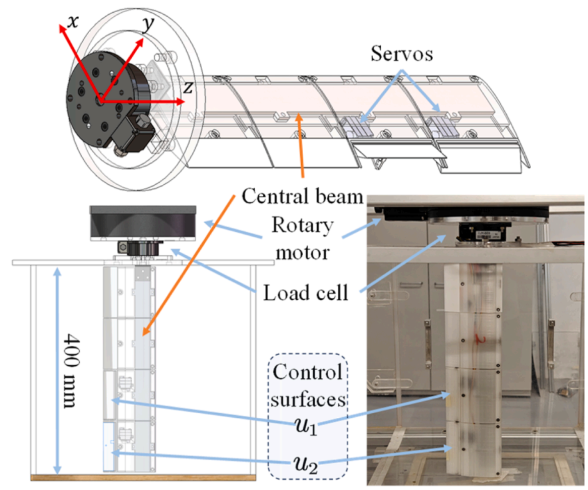

Fig. 2. Flexible wing design and installation in the wind tunnel.

Table 2
Digital servo parameters.

Parameters	Values
Operational speed	0.08 s/60°
Stall torque	3.2 kg·cm
Dimension	23.5 × 8 × 23.4 mm
Weight	11 g

Table 3
Load cell specifications.

Measurement	Range	Resolution
F_x, F_y	±600 N	0.06 N
F_z	±800 N	0.08 N
M_x, M_y, M_z	±15 N·m	0.0015 N·m

In the wind tunnel experiments, the load cell and servos were sensed and controlled in real-time with the Beckhoff TwinCAT system via EtherCAT and RS485 communications at a 200 Hz sampling rate. Servos were calibrated via the KEYENCE LK-503 1D profiler to establish the nonlinear relationship between the control surface deflection in degree and the servo duty cycle in percentage.

4.2. Flexible wing LPV-NG system identification via wind tunnel data

To connect to the LPV-NG system defined in Section 2, the control surface deflections are defined as the control input $u = \{u_1 \quad u_2\}^\top$. The term ρ defined in Eq. (4) and subsequent equations is the low-frequency control surface input u_l. The output of the FW is defined as

$$y = \{ M_x \quad L_y \}^\top, \tag{38}$$

which are equivalent to the defined flexible response y_f and rigid-body response y_r.

The model's nonlinearity roots from two primary sources: 1) the nonlinear relationship between control surface inputs and aerodynamic loads due to geometric deformations of the FW, and 2) the nonlinear bending moments caused by different distances of control surfaces from the wing root, despite uniform aerodynamic coefficients on all airfoil sections. This nonlinear behavior is experimentally captured and represented by a nonlinear function defined in Eq. (3).

To establish a static portion of the LPV-NG model, static responses of the FW acquired from the control surface deflections $\pm 20^\circ$ with 4° increments were sampled at a wind speed of 22 m/s. The bending moment and lift experimental data with a Non-uniform rational B-spline (NURBS) surface parameterization and their Jacobian data are shown in Fig. 3 and Fig. 4. The NURBS fitting reached $R^2 = 95.7\%$, indicating the desired fitting performance of the static nonlinear function.

The dynamic wind tunnel test is to identify the LPV model using a two-step frequency domain method. The first identification step extracts the Laplace transform of the time-domain input-output dynamic wind tunnel data, with control surface deflections as inputs, and flexible and rigid outputs from the load cell as outputs. The second step involves model identification of linear state-space models from the extracted frequency responses. Wind tunnel tests included a sinusoidal excitation to control surfaces from several constant angles as

$$\begin{aligned} u_{1j}(t) &= A_{1i}\sin(\omega_i t) + A_{10j}, \\ u_{2j}(t) &= A_{2i}\sin(\omega_i t) + A_{20j}, \end{aligned} \tag{39}$$

where ω_i is the excitation frequencies, A_{1i} and A_{2i} are the shrinking excitation amplitudes to ensure the motor has sufficient torque. The selection of frequencies and amplitudes is shown in Fig. 5. A_{10j} and A_{20j} describe the offset angle introduced to the control surfaces.

From practical FW use cases, the LA application typically starts from a scenario where the outer control surface supports all the control actions. Therefore, $\{A_{10j}\ A_{20j}\}^\top$ is only chosen from the three static deflections $\{0\ 0\}^\top$, $\{0\ 5\}^\top$, and $\{0\ 10\}^\top$. The dynamic excitations are introduced based on top of these static deflections. A complete dynamic test consists of two sub-tests. In the first sub-test, a sinusoidal signal with a specified amplitude, frequency, and offset angle is applied to the inner control surface, while the outer control surface is held stationary at offset angle A_{20j}. The second sub-test involves alternating the signal input between the inner and outer control surfaces. The output of the locally identified linear time-invariant (LTI) model is solely dependent on increases from the offset angle $\{A_{10j}\ A_{20j}\}^\top$ i.e.,

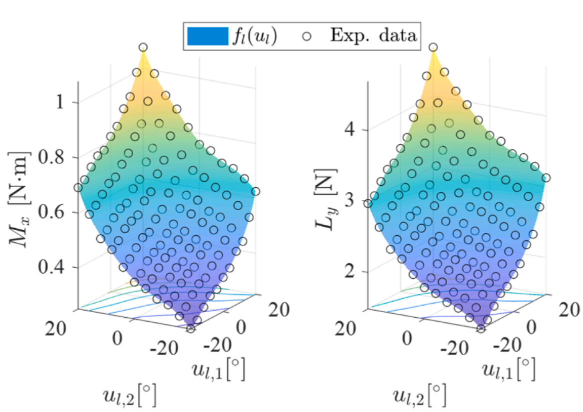

Fig. 3. The bending moment and lift of flexible wing and its NURBS parameterization from static wind tunnel test.

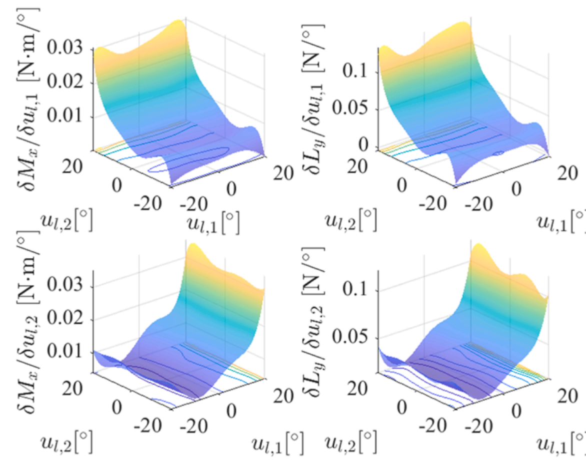

Fig. 4. The Jacobian of bending moment and lift with respect to control surfaces input and its NURBS parameterization.

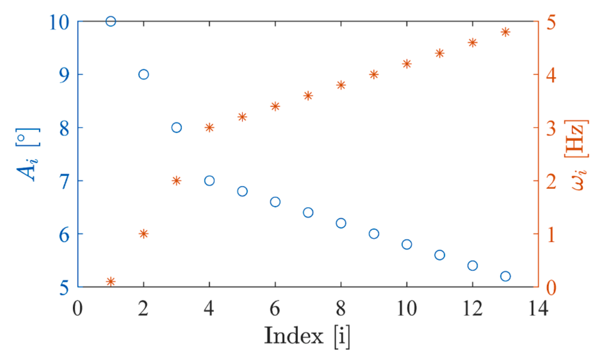

Fig. 5. Amplitude and frequency input sets for dynamic LPV-NG system identification.

$$\Delta y_j(t) = y_j(t) - f_l(\rho_j), \tag{40}$$

where $\rho_j = \{ A_{10_j} \quad A_{20_j} \}^\top$.

The input $U(s,\rho_j)$ and output $\Delta Y(s,\rho_j)$ are the Laplace transform of $u_j(t)$ and $\Delta y_j(t)$ defined in Eq. (39) and Eq. (40), respectively. A multiple-input multiple-output (MIMO) sub-model is constructed around control surface offset ρ_j via decomposition to multiple single-input single-output (SISO) systems i.e.,

$$\begin{aligned} U(s,\rho_j) &:= \begin{bmatrix} U_1(s,\rho_j) \\ U_2(s,\rho_j) \end{bmatrix}, \\ \Delta Y(s,\rho_j) &:= \begin{bmatrix} \Delta Y_{M_x,1}(s,\rho_j) & \Delta Y_{M_x,2}(s,\rho_j) \\ \Delta Y_{L_y,1}(s,\rho_j) & \Delta Y_{L_y,2}(s,\rho_j) \end{bmatrix}, \end{aligned} \tag{41}$$

where subscripts 1 and 2 representing ΔY_{M_x} or ΔY_{L_y} are obtained from the case of the corresponding control surfaces oscillating at a given amplitude and frequency. Four sets of SISO frequency response data were generated as

$$\begin{cases} G_{11}(s,\rho_j) = \dfrac{\Delta Y_{M_x,1}(s,\rho_j)}{U_1(s,\rho_j)}, G_{12}(s,\rho_j) = \dfrac{\Delta Y_{M_x,2}(s,\rho_j)}{U_2(s,\rho_j)}, \\ G_{21}(s,\rho_j) = \dfrac{\Delta Y_{L_y,1}(s,\rho_j)}{U_1(s,\rho_j)}, G_{22}(s,\rho_j) = \dfrac{\Delta Y_{L_y,2}(s,\rho_j)}{U_2(s,\rho_j)}. \end{cases} \tag{42}$$

Therefore, one of the sub-models was acquired as

$$G_j(s,\rho_j) = \begin{bmatrix} G_{11j}(s,\rho_j) & G_{12j}(s,\rho_j) \\ G_{21j}(s,\rho_j) & G_{22j}(s,\rho_j) \end{bmatrix}, \tag{43}$$

Multiple experiments were performed to obtain three sub-models at each offset angle. The LTI model $G(s)$ was acquired via the model average principle to three sub-models. The generation of $G(s)$ may be slightly different based on the offset angle selected. The current approach takes averages among these estimations.

The nonlinear effectiveness is acquired from the averaged model and FW static response as

$$f(u_l) = G(0)^{-1} J_l(u_l), \tag{44}$$

where $G(0)$ is defined as the DC gain of the LTI model $G(s)$. Note that nonlinear effectiveness alters the input of Eq. (41) as $\widetilde{U}_h(s,\ \rho_j)\ = f(\rho_j)U_h(s)$, and the local identification processes from Eq. (41) to Eq. (43) are repeated to obtain three normalized sub-models $G_n(s,\rho_0)$, $G_n(s,\rho_5)$, and $G_n(s,\rho_{10})$. The main goal of $f(u_l)$ is to minimize the gap between LTI models. The bode plot in Fig. 6 demonstrates successful normalization of sub-models via merging into one line, indicating the proposed decomposition in Eq. (41) is a reasonable description. This also guarantees the compatibility condition in Eq. (5).

In addition, the nonlinear effectiveness is added to the averaged LTI model $G(s)$ as

$$G_h(s,\rho_j) = G(s)f(\rho_j). \tag{45}$$

Three additional models $G_h(s,\rho_0)$, $G_h(s,\rho_5)$, and $G_h(s,\rho_{10})$ were obtained. It is shown in Fig. 6 that this format predicts frequency responses very well at different offset angles and matches with experimental data. This indicates that the parameter of the LPV system in Eq. (4) only has varying terms on the control effectiveness matrices. Therefore, the LPV system is simplified to

$$Y_h(s) = G(s)f(u_l)U_h(s), \tag{46}$$

where $U_h(s)$ and $Y_h(s)$ are the Laplace transform of $u_h(t)$ and $y_h(t)$ defined in Eq. (4), respectively.

The verification of the proposed LPV-NG system is highlighted in the frequency response plot shown in Fig. 6. The offsets of the frequency response data are well predicted with the established LPV-NG model. It's worth noting that the peak in Fig. 6 represents the first aeroelastic mode of the FW prototype, which is sufficiently high to justify the frequency separation assumption. Additionally, a 2 Hz low-pass Butterworth filter applied to control inputs effectively decouples aeroelastic and rigid-body modes, further reinforcing the robustness of the frequency separation assumption in this study. Moreover, the LPV uncertainty is evaluated by comparing the identified model with experimental data in the frequency domain, demonstrating high phase agreement. This phase alignment is critical for robust null space modeling, as it ensures accurate capture of dynamic interactions, minimizes representation errors and maintains stability while avoiding performance degradation [48].

4.3. Simulation verification of nonlinear-control-allocation load alleviation

From practical FW use cases, it is assumed that the FW control is generated to track a given trajectory that transitions from a trimmed flight to the climbing phase. This trajectory is selected as it typically introduces excessive load to the structure. Two trajectories are simulated in this subsection, including

- Flight Condition I: Wind speed 22 m/s, $u_{0,2}$ is defined as a trapezoidal signal with a maximum 12°°, and the body angle of attack 2°°
- Flight Condition II: Wind speed 30 m/s, $u_{0,2}$ is defined as a trapezoidal signal with a maximum 14°°, and body angle of attack 2°

It is expected that the maximum wing-root bending moment M_x is reduced by 10% with the proposed CNCA method while achieving minimum change of the rigid-body output L_y and least flexible load violation.

In this framework, the single rigid-body output and the dual control surface input formulate a redundant system, as defined in Eq. (8). Accordingly, the corresponding LPV-NG IM in Section 3 is established, where the flexible output is expected to be minimized. Therefore, the feedback controller C is designed as a proportional-integral-derivative (PID) controller. The desirable flexible response r is constructed to satisfy a 10% reduction at the climb stage, yielding the proxy signal v, as described in Eq. (24).

To show the effectiveness of the proposed methods, four different control allocation methods are compared. They are:

- Proposed CNCA,
- Proposed NCA,

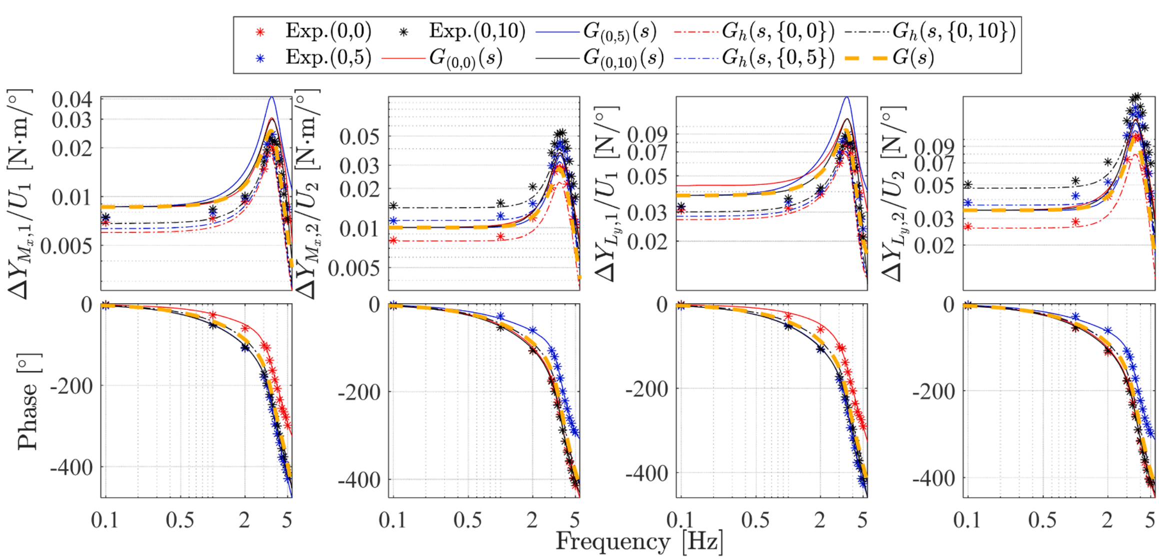

Fig. 6. Flexible wing LPV-NG system verification with dynamic wind tunnel experiment data, normalized sub-models $G_n(s,\rho_j)$, and the high-frequency portion of the LPV-NG model $G_h(s,\rho_j)$.

- Compensated static control allocation (CSCA) that consists of the static CA method [34] and proposed static compensator μ_c in Eq. (14), and
- Dynamic control allocation (DCA) [33] with LPV model only.

These four methods all exploit the invariant manifold structure via proxy signals. Therefore, they generate separate v signals with dedicated controllers. Note that LA input u_N will be disconnected from the system at the end of the climb phase.

The flexible and rigid output from simulations of MLA under Flight Condition I is shown in Fig. 7. All four methods achieve LA within 10 s, indicating similar closed-loop bandwidth across the controllers. However, differences are observed in their responses to flexible load violations and rigid output performance. The DCA exhibits the largest peak values for both outputs, primarily due to delays in the dynamic IM response. Conversely, CNCA displays the smallest peak values, demonstrating the effectiveness of the OICC algorithm in manipulating the proxy signal. This is further evidenced in Fig. 8, where the allocated input $u_{N,2}$ of DCA shows the smallest slope and is triggered last, whereas CNCA exhibits more aggressive control efforts in $u_{N,2}$. The performance of the CSCA and NCA were similar before high-frequency excitation was added to the simulation, as indicated by comparable patterns and magnitudes in control allocation inputs. However, DCA differs in control inputs and rigid steady-state value, due to the limitations of only using the LPV system and dynamic IM to capture low-frequency nonlinearity.

The simulation incorporates 4 Hz sinusoidal excitations from 15 s to 22 s., as depicted in Fig. 7 and Fig. 8, revealing significant differences in the impact on lift across all four cases. The CSCA method only maintains CA effectiveness when the proxy signal v comprises only low-frequency components. However, with high-frequency excitations, the static IM fails, leading to noticeable oscillations in rigid-body output. In contrast, the DCA method exhibits a reduction in the magnitude of high-frequency excitations relative to the CSCA method. The proposed NCA and CNCA methods introduce the smallest variations in rigid-body responses throughout both the static and dynamic portions of the simulation. This confirms that the proposed methods, which utilize a decomposed IM for the LPV-NG system, effectively perform the MLA task without compromising the performance of the rigid-body responses.

The advantages of IM decomposition and the impact of flexible output constraints are highlighted in Fig. 9. The figure is organized into

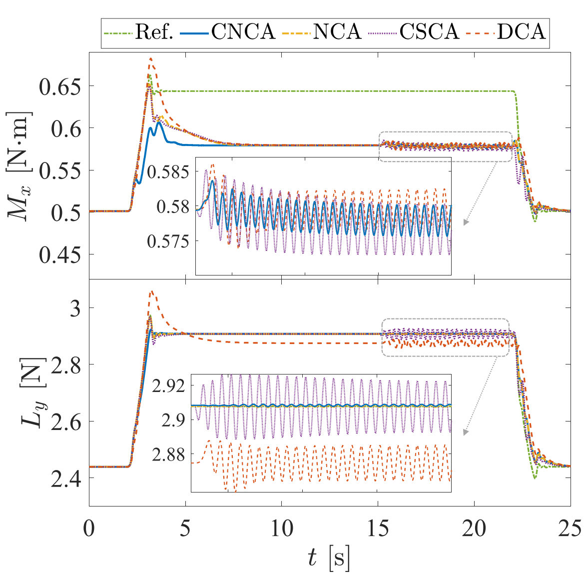

Fig. 7. The wing root bending moment and lift of flight trajectory compared with control allocation methods of DCA, CSCA, NCA, and CNCA in Flight Condition I. A 4 Hz sinusoidal excitation is added to the proxy signal v at 15 s.

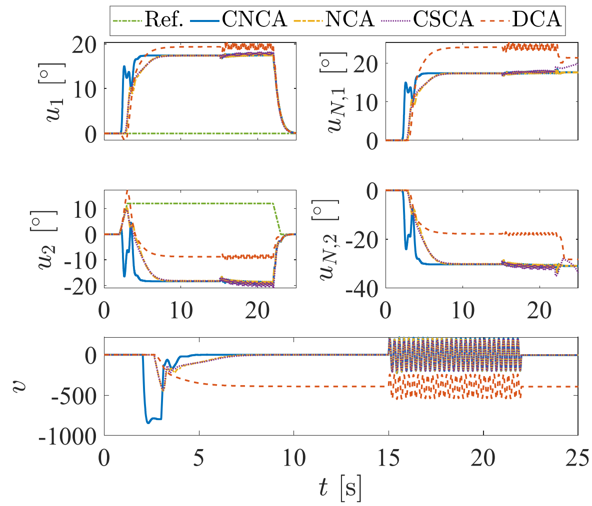

Fig. 8. Comparison of input u, allocated input u_N, and proxy signal v in Flight Condition I.

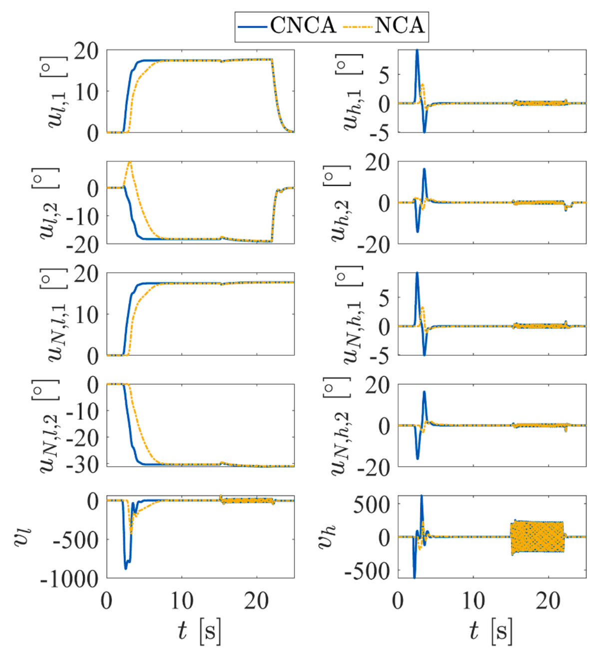

Fig. 9. Comparison of high-frequency and low-frequency input u, allocated input u_N, and proxy signal v for NCA, and CNCA cases in Flight Condition I.

two columns: the left and right column displays the low-frequency and high-frequency components of the LPV-NG model input, allocated input, and proxy signal, respectively. This decomposition demonstrates the effective filtration of high-frequency sinusoidal excitation, enabling the low-frequency IM to function within its optimal frequency range; therefore it avoided significant oscillations in the rigid output as depicted in Fig. 7. Furthermore, the implementation of a flexible output constraint significantly reduced the peak load from 0.651 Nm in the NCA scenario to 0.606 Nm, achieving a 59.7% reduction in load violation relative to the desirable load reference. This reduction is facilitated by control allocation responses that effectively counteract control inputs u_0, thereby decreasing flexible load while preserving rigid-body response performance. In addition, the wingtip displacement is directly correlated with the load. The maximum wingtip deflection remained below 15% of the FW prototype's semi-span, as observed in the wind tunnel experiment.

The simulation of Flight Condition II is illustrated in Fig. 10–Fig. 12. All methods reduced 10% flexible output at higher flow speeds and control inputs. The DCA consistently exhibited the highest peak values and altered rigid steady-state values, attributed to the limitations of solely using the LPV system and dynamic IM inaccurately capturing the low-frequency nonlinearity of the FW. Conversely, the CNCA demonstrated the lowest peak values for both rigid and flexible outputs, reducing the peak load from the NCA case of 1.273 Nm to 1.173 Nm, equating to a 69.4% load violation reduction with respect to the desirable flexible load reference. This effect is highlighted in Fig. 12, where allocated input effectively counteracts control input, enhancing safety and comfort for passengers. Similar to the previous case, NCA and CNCA resulted in minimal sinusoidal oscillation in the rigid output.

The main difference between the two flight conditions is the additional vibration caused by a larger magnitude of control inputs during the climb stage. As the load increases, the magnitude of the proxy signal significantly increases for CSCA, NCA, and CNCA, leading to increased vibration of control allocation input as presented in Fig. 11. The additional force output vibration is shown in Fig. 10. Moreover, flexible output saturation in Fig. 12 demonstrates oscillation suppression of the proposed CNCA method, which displays a reduction of high-frequency oscillation during the climb stage with respect to NCA.

4.4. Wind tunnel test verification of load alleviation

The wind tunnel experiment was also conducted at the wind tunnel of the HKUST AAF with the same hardware setup. The flow speed and body angle of attack were 22 m/s and 2°° respectively. As in the simulation, allocated input u_N was disconnected from the system at the end of the climb phase. The saturation bounds of control surfaces u were limited to $\pm 20^\circ$ to ensure digital servos are within the normal operational range.

The LA evaluation period spanned from 3.25 s to 21 s, based on the load cell reading during the climb phase when the flexible output began exceeding the desirable load reference. The error for bending load and lift is introduced as

$$\begin{aligned} e_{M_x} &= M_x - r, \\ e_{L_y} &= L_y - L_{y_0}, \end{aligned} \tag{47}$$

where M_x and L_y are the load cell outputs from wind tunnel experiments. Term L_{y_0} is the lift force without CA. Term r is a desirable flexible

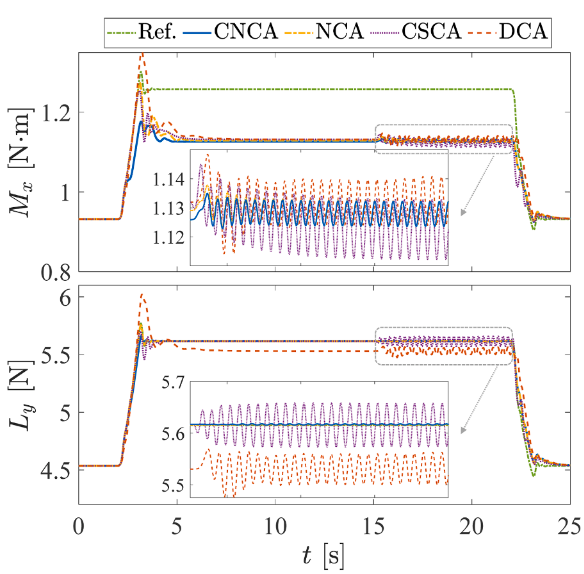

Fig. 10. The wing root bending moment and lift of flight trajectory in Flight Condition II.

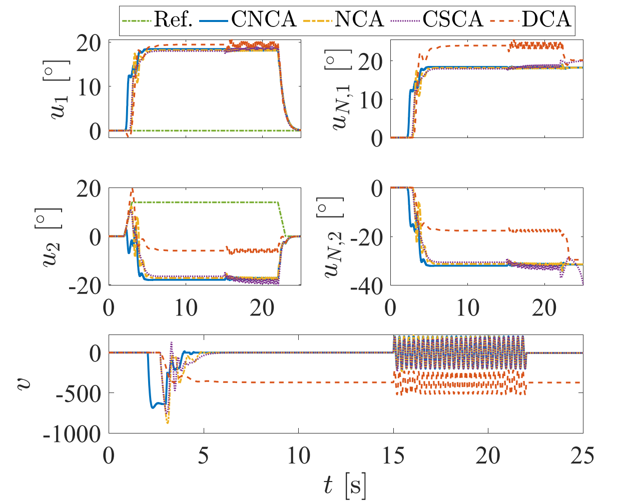

Fig. 11. Comparison of input u, allocated input u_N, and proxy signal v in Flight Condition II.

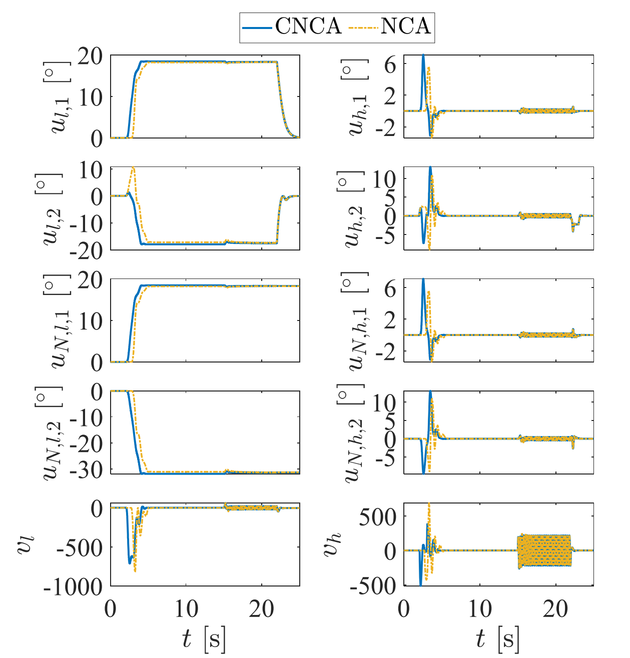

Fig. 12. Comparison of high-frequency and low-frequency input u, allocated input u_N, and proxy signal v in Flight Condition II.

response reference defined in Eq.(24). The quantified evaluation is listed in Table 4. The * indicates the proposed method.

The load cell reading of wind tunnel tests is presented in Fig. 13. CNCA, NCA, and CSCA completed the LA within 10 s. However, their performances during the LA process and steady-state values vary. The DCA exhibited the largest peak load due to dynamic IM lagging and the highest steady-state error for both flexible and rigid outputs, as reflected

Table 4
Wind tunnel load alleviation performance evaluation.

Method	$\Vert e_{M_x} \Vert_\infty$ (N·mm)	$\Vert e_{M_x} \Vert_\infty$ (%)	$\Vert e_{M_x} \Vert_2$ (N·mm)	$\Vert e_{L_y} \Vert_2$ (N)
CNCA*	16.7	−75.9	6.5	0.050
NCA*	69.2	0	15.7	0.043
CSCA*	71.4	+2.9	15.8	0.044
DCA [33]	119.3	+72.4	35.9	0.091

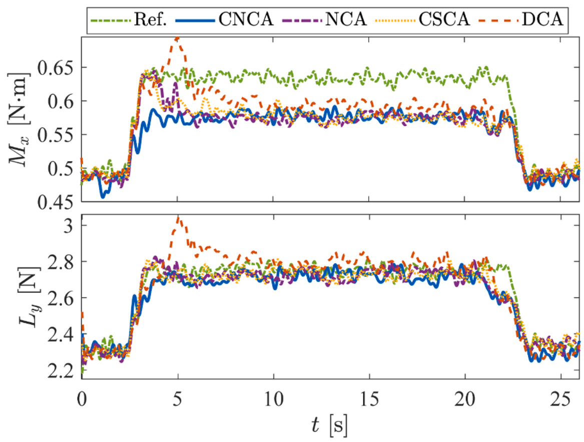

Fig. 13. Load cell data of flexible wing wind tunnel load alleviation experiment at flight condition of the wind speed 22 m/s, body angle of attack 2°, and max pilot input 12°.

by the largest infinity-norms and 2-norms values. This error arises from the saturation limit imposed on the control surface u, as illustrated in Fig. 14, where DCA's control surface reaches a 20° limit, but does not achieve the LA, prompting continued excessive control efforts $u_{N,1}$ up to 50°. This saturation is consistent with simulation results indicating that control inputs need to exceed 20° to accomplish LA. The CSCA and NCA cases demonstrate similar trends in both load types and norms analysis, indicating that the wind tunnel environment is dominated by low frequencies. Despite that, both cases experienced undesirable load violations on the flexible load. In contrast, the proposed CNCA method effectively minimizes load violations by activating the proxy signal 0.5 s earlier and more aggressively than the other methods, reducing 75.9% in load violations with respect to NCA, as shown in Table 4, Fig. 14 and Fig. 15. However, a minor trade-off between load violation suppression and tracking performance is noted in CNCA, where the rigid load slightly underperformed the reference between 3.25 s to 6 s, resulting in a higher 2-norms value for the rigid output of CNCA compared to NCA. Fig. 15 highlights the enhanced suppression of flexible load violations in CNCA through more aggressive high-frequency control inputs.

In summary, the proposed CNCA method accomplishes MLA and load violation suppression with minimal impact on the rigid-body output during wind tunnel verification tests. Furthermore, wind tunnel tests demonstrate the LPV-NG model precisely captures the dynamic and static responses of the FW prototype, as evidenced by the congruent trends observed in the load cell output and allocated inputs from both

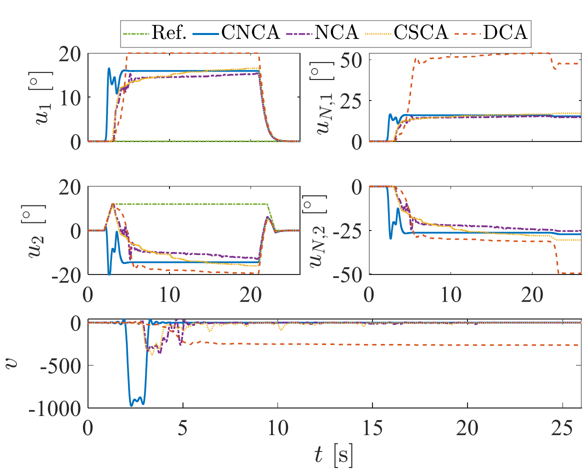

Fig. 14. Comparison of input u, control allocation input u_N, and proxy signal v of flexible wing wind tunnel experiment.

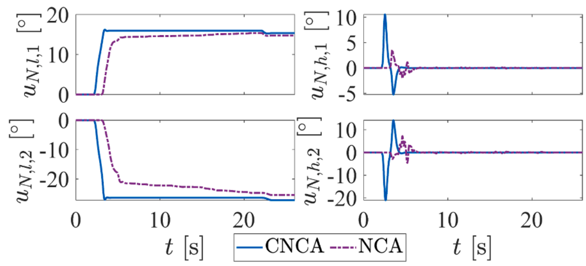

Fig. 15. Comparison of the high-frequency and low-frequency portions of the input u and control allocation input u_N of the flexible wing wind tunnel experiments.

wind tunnel and simulation studies.

5. Conclusion

This paper proposes a novel decoupled CNCA framework to enhance dynamic MLA performance. The framework models input-redundant FA as an LPV-NG, preserving dynamic properties of FA via conventional LPV models and capturing static nonlinearity with static nonlinear functions. Control allocation decoupling is achieved by an IM structure that considers both high-frequency and low-frequency relationships of the FA, ensuring that the proxy signal does not impact the rigid-body response while reducing structural load at critical locations. Additionally, flexible load constraint is implemented to further minimize structural load violations. The effectiveness of the proposed method was validated using a FW prototype, with aerodynamic data gathered from wind tunnel tests to show its compliance with the LPV-NG model. The proposed CNCA method compares with existing allocation methods to show its effectiveness in reducing load violation and mitigating high-frequency disturbances without compromising rigid-body responses, as shown via simulation and wind tunnel experiments.

CRediT authorship contribution statement

Boge Dong: Writing – review & editing, Writing – original draft, Visualization, Validation, Software, Methodology, Investigation, Formal analysis, Data curation, Conceptualization. **Yi Zhou:** Validation, Software, Data curation. **Molong Duan:** Writing – review & editing, Supervision, Project administration, Funding acquisition, Conceptualization.

Declaration of competing interest

The authors declare that they have no known competing financial interests or personal relationships that could have appeared to influence the work reported in this paper.

Acknowledgements

The authors acknowledge support from the Innovation and Technology Fund (GHP/170/22SZ). Mr. Sam Wong and Dr. Ryu Fattah provided valuable feedback to this work. The help from other researchers is sincerely appreciated. The authors acknowledge support from the Research Grants Council (RGC) of the Government of Hong Kong Special Administrative Region (HKSAR) with RGC/ECS Project (No. 26215824), the Frontier Technology Research for Joint Institutes with industry scheme under grant OKT24EG07, as well as the HKUST – HKUST(GZ) Cross-campus Collaborative Research Scheme under the Great Bay Area "1 + 1 + 1″ Joint Funding Program. This work was supported in part by the Project of Hetao Shenzhen-Hong Kong Science and Technology Innovation Cooperation Zone (HZQB-KCZYB-2020083).

Data availability

Data will be made available on request.

References

[1] Resolution on the industry's commitment to reach net zero carbon emissions by 2050, Int. Air Transp. Assoc. (2021). Oct. 04, https://www.iata.org/en/programs/environment/flynetzero (accessed Jun. 21, 2024).
[2] M. Duan, J.H. Hansen, I.V. Kolmanovsky, C.E.S. Cesnik, Maneuver load alleviation of flexible aircraft through control allocation: a case study using X-HALE, Int. Forum Aeroelast. Struct. Dynam. (IFASD 2019) (Jun. 2019).
[3] A.F. Arrieta, I.K. Kuder, M. Rist, T. Waeber, P. Ermanni, Passive load alleviation aerofoil concept with variable stiffness multi-stable composites, Compos. Struct. 116 (1) (Sep. 2014) 235–242.
[4] W.D.K. Cavens, A. Chopra, A.F. Arrieta, Passive load alleviation on wind turbine blades from aeroelastically driven selectively compliant morphing, Wind Energy 24 (1) (Jan. 2021) 24–38.
[5] M. Ahmadi, T. Farsadi, H.Haddad Khodaparast, Enhancing gust load alleviation performance in an optimized composite wing using passive wingtip devices: folding and twist approaches, Aerosp. Sci. Technol. 147 (Apr. 2024) 109023.
[6] Y. Bi, C. Xie, C. An, C. Yang, Gust load alleviation wind tunnel tests of a large-aspect-ratio flexible wing with piezoelectric control, Chin. J. Aeronautics 30 (1) (Feb. 2017) 292–309.
[7] S. Basualdo, Load alleviation on wind turbine blades using variable airfoil geometry, Wind Eng. 29 (2) (Mar. 2005) 169–182.
[8] I. Dimino, G. Andreutti, F. Moens, F. Fonte, R. Pecora, A. Concilio, Integrated design of a morphing winglet for active load control and alleviation of turboprop regional aircraft, Appl. Sci. 11 (5) (Mar. 2021) 2439.
[9] D.B. Doman, A.G. Sparks, Concepts for constrained control allocation of mixed quadratic and linear effectors, in: Proceedings of the 2002 American Control Conference (IEEE Cat. No.CH37301), 2002, pp. 3729–3734.
[10] O. Härkegård, S.T. Glad, Resolving actuator redundancy—Optimal control vs. control allocation, Automatica 41 (1) (Jan. 2005) 137–144.
[11] A. Cristofaro, S. Galeani, Output invisible control allocation with steady-state input optimization for weakly redundant plants, in: 53rd IEEE Conference on Decision and Control, Dec. 2014, pp. 4246–4253.
[12] Y. Zhou, M. Duan, Vibration compensation of an extendable variable-stiffness boom-lift-mounted robot, IEEE/ASME Trans. Mechatron. 29 (4) (Aug. 2024) 2812–2820.
[13] R.J. White, Improving the airplane efficiency by use of wing maneuver load alleviation, J. Aircr. 8 (10) (Oct. 1971) 769–775.
[14] Y. Yang, Z. Wu, C. Yang, Control surface efficiency analysis and utilization of an elastic airplane for maneuver loads alleviation, in: 54th AIAA/ASME/ASCE/AHS/ASC Structures, Structural Dynamics, and Materials Conference, Apr. 2013.
[15] S. Haghighat, H.H.T. Liu, J.R.R.A. Martins, Model-predictive gust load alleviation controller for a highly flexible aircraft, J. Guid., Contr. Dynam. 35 (6) (Nov. 2012) 1751–1766.
[16] B. Barzgaran, J.D. Quenzer, M. Mesbahi, K.A. Morgansen, E. Livne, Real-time model predictive control for gust load alleviation on an aeroelastic wind tunnel test article, AIAA Scitech 2021 Forum (January) (Jan. 2021) 1–18.
[17] M.F.V Pereira, M. Duan, C.E.S. Cesnik, F. Vetrano, Model predictive control for very flexible aircraft based on linear parameter varying reduced-order models, in: Proceedings of International Forum on Aeroelasticity and Structural Dynamics (IFASD 2022), 2022, pp. 1–18.
[18] X. Liu, Q. Sun, J.E. Cooper, LQG based model predictive control for gust load alleviation, Aerosp. Sci. Technol. 71 (Dec. 2017) 499–509.
[19] L. Burlion, C. Poussot-Vassal, P. Vuillemin, M. Leitner, T. Kier, Longitudinal manoeuvre load control of a flexible large-scale aircraft, IFAC Proc. Vol. 47 (3) (2014) 3413–3418.
[20] Z. Qu, A.M. Annaswamy, Adaptive output-feedback control with closed-loop reference models for very flexible aircraft, J. Guid., Cont. Dynam. 39 (4) (Apr. 2016) 873–888.
[21] M. Lanchares, I. Kolmanovsky, C.E.S. Cesnik, F. Vetrano, Model order reduction for coupled nonlinear aeroelastic-flight mechanics of very flexible aircraft, in: International Forum on Aeroelasticity and Structural Dynamics (IFASD 2019), Jun. 2019.
[22] D.K. Schmidt, D.L. Raney, Modeling and simulation of flexible flight vehicles, J. Guid. Contr. Dynam. 24 (3) (2001) 539–546.
[23] I. Tuzcu, Dynamics and control of flexible aircraft, Virginia Tech (2001).
[24] C.E.S. Cesnik, R. Palacios, E.Y. Reichenbach, Reexamined structural design procedures for very flexible aircraft, J. Aircr. 51 (5) (Sep. 2014) 1580–1591.
[25] C.M. Shearer, C.E.S. Cesnik, Nonlinear flight dynamics of very flexible aircraft, J. Aircr. 44 (5) (Sep. 2007) 1528–1545.
[26] M.C. van Schoor, A.H. von Flotow, Aeroelastic characteristics of a highly flexible aircraft, J. Aircr. 27 (10) (Oct. 1990) 901–908.
[27] A. del Carre, A. Muñoz-Simón, N. Goizueta, R. Palacios, SHARPy: a dynamic aeroelastic simulation toolbox for very flexible aircraft and wind turbines, J. Open. Source Softw. 4 (44) (Dec. 2019).
[28] C.M. Shearer, C.E.S. Cesnik, Trajectory control for very flexible aircraft, J. Guid., Contr., Dynam. 31 (2) (2008) 340–357.
[29] M. Duan, C.E.S. Cesnik, I.V. Kolmanovsky, F. Vetrano, Control-oriented modeling for flexible aircraft, J. Aircr. 61 (1) (Jan. 2024) 183–195.
[30] M. Duan, C.E. Cesnik, I.V. Kolmanovsky, F. Vetrano, Nonlinear control-oriented modeling for very flexible aircraft, AIAA Scitech 2021 Forum (Jan. 2021).
[31] P.S. Zink, D.N. Mavris, D.E. Raveh, Maneuver trim optimization techniques for active aeroelastic wings, J. Aircr. 38 (6) (Nov. 2001) 1139–1146.
[32] S.A. Frost, M. Bodson, J.J. Burken, C.V. Jutte, B.R. Taylor, K.V. Trinh, Flight control with optimal control allocation incorporating structural load feedback, J. Aerospace Inform. Syst. 12 (12) (Dec. 2015) 825–834.
[33] J.H. Hansen, Control allocation of flexible aircraft for load alleviation, Univ. Michigan (2021).
[34] L. Zaccarian, Dynamic allocation for input redundant control systems, Automatica 45 (6) (Jun. 2009) 1431–1438.
[35] F. Saltari, C. Riso, G. De Matteis, F. Mastroddi, Finite-element-based modeling for flight dynamics and aeroelasticity of flexible aircraft, J. Aircr. 54 (6) (Nov. 2017) 2350–2366.
[36] F.J. Silvestre, A.B. Guimarães Neto, R.M. Bertolin, R.G.A. da Silva, P. Paglione, Aircraft control based on flexible aircraft dynamics, J. Aircr. 54 (1) (Jan. 2017) 262–271.
[37] I. Piacenza, G. Avanzini, E. Capello, Mixed newtonian-lagrangian approach for the analysis of flexible aircraft dynamics, in: AIAA Atmospheric Flight Mechanics Conference, Aug. 2011.
[38] R. Palacios, J. Murua, R. Cook, Structural and aerodynamic models in nonlinear flight dynamics of very flexible aircraft, AIAA J. 48 (11) (Nov. 2010) 2648–2659.
[39] M. Duan, C.E. Okwudire, Connections between control allocation and linear quadratic control for weakly redundant systems, Automatica 101 (Mar. 2019) 96–102.
[40] M. Duan, I.V. Kolmanovsky, C.E. Cesnik, Maneuver load alleviation of very flexible aircraft via nonlinear decoupling control, AIAA Scitech 2021 Forum (Jan. 2021).
[41] L. Burlion, A new saturation function to convert an output constraint into an input constraint, in: 2012 20th Mediterranean Conference on Control & Automation (MED), Jul. 2012, pp. 1217–1222.
[42] J. Piquee, I. López Canalejo, C. Breitsamter, R. Wüchner, K.-U. Bletzinger, Aerodynamic analysis of a generic wing featuring an elasto-flexible lifting surface, Adv. Aerodynam. 1 (1) (Dec. 2019) 20.
[43] J.-W. Lee, J.-H. Han, H.-K. Shin, H.-J. Bang, Active load control of wind turbine blade section with trailing edge flap: wind tunnel testing, J. Intell. Mater. Syst. Struct. 25 (18) (Dec. 2014) 2246–2255.
[44] R. Castro-Triguero, S. Murugan, R. Gallego, M.I. Friswell, Robustness of optimal sensor placement under parametric uncertainty, Mech. Syst. Signal. Process. 41 (1–2) (Dec. 2013) 268–287.
[45] Y. Zhao, J. Du, H. Bao, Q. Xu, Optimal sensor placement for inverse finite element reconstruction of three-dimensional frame deformation, Int. J. Aerospace. Eng. 2018 (2018).
[46] M. Gherlone, P. Cerracchio, M. Mattone, M. Di Sciuva, A. Tessler, Shape sensing of 3D frame structures using an inverse Finite element method, Int. J. Solids. Struct. 49 (22) (Nov. 2012) 3100–3112.
[47] W.L. Ko, L. Richards, and V.T. Fleischer, "Applications of KO displacement theory to the deformed shape predictions of the doubly-tapered Ikhana Wing," 2009. [Online]. Available: http://www.sti.nasa.nov.
[48] Zhou Kemin, J.C. Doyle, K. Glover, Robust and Optimal Control, 2, Prentice Hall, 1996.